Supplement of Biogeosciences, 22, 6937–6962, 2025
https://doi.org/10.5194/bg-22-6937-2025-supplement

Biogeosciences
Open Access

Supplement of

Evaluating the carbon and nitrogen cycles of the QUINCY terrestrial biosphere model using space-born optical remotely-sensed data

Tuuli Miinalainen et al.

Correspondence to: Tuuli Miinalainen (tuuli.miinalainen@fmi.fi)

Contents of this file

1. Section S1

2. Tables S1 to S12

3. Figures S1 to S13

S1 Description of *in-situ* data collection for FI-Sod and US-NR1

To determine the chlorophyll content of the crowns in Sodankylä, there were taken in total 160 biweekly needle samples from the south and north faces of crowns of three mature Scots pine (*Pinus sylvestris*) trees during 31.3–30.9.2015. Needle samples were taken separately for one- and three-year-old shoots of branches that were cut with clippers from the upper part of the crowns. Each sample consisted of four pairs of needles that were immediately immersed in liquid nitrogen in a portable dewar (CX-100, Taylor Wharton International LLC, Minnetonka, MN), and subsequently stored at -80 $^{\circ}\mathrm{C}$ until extraction. Pigments were analysed by using a method following Wellburn (1994) with dimethyl sulfoxide (VWR Chemicals, 23500.322) as solvent. Frozen needle samples (75—100 mg) were first homogenized for 2 minutes at 30 Hz, using a bead mill (TissueLyser II Qiagen, Germany), stainless steel beads (4 mm), and microtubules (2 ml). Subsequently, 1.8 ml of dimethyl sulfoxide was added to the homogenate and resuspended again at 30 Hz for one minute. Pigments were extracted in oven at 40 $^{\circ}\mathrm{C}$ for 4 hr. The extracts were then centrifuged at 25000 g for five minutes. Light absorption was measured at 649.1, 665.1, and 480.0 nm, with a spectrophotometer (Shimadzu UV-2401 PC), and subsequently used in the estimation of chl A, chl B, and total carotenoids (Wellburn, 1994). The Sodankylä $\mathrm{chl_{leaf}}$ measurements represent both chlorophyll A and B ($\mathrm{chl_{a+b}}$).

The US-NR1 pigment measurements represent two tree species: lodgepole pine (*Pinus contorta*) and Engelmann spruce (*Picea engelmannii*). The measurements were collected from tree branches and the pigments were extracted in solvent, and then analyzed by liquid chromatography (Bowling and Logan, 2019). We calculated the daily average value of $\mathrm{chl}_{\mathrm{leaf}}$ over measurements from several trees, and filtered out the days when fewer than three samples were available.

For FI-Sod, we also used *in-situ* measurement data for the fraction of absorbed photosynthetic radiation (fAPAR) for the years 2021–2024 which were measured with the PQS1 instrument with factory calibration (Knorr et al., 2025). We excluded those days from *in-situ* fAPAR measurements for which the 2021–2024 daily mean photosynthetically active radiation (PAR) below canopy was less than one. This was done in order to filter out measurement data that might not be representative due to reduced sun light and potential snow cover.

Table S1. A list of data sets used in the study.

Sites	Location	Time interval	Type & variables	Source
QUINCY simulation input				
PLUMBER2	global	1992–2018	meteorological data	Ukkola et al. (2022)
GLOBAL	global	1989–2018	meteorological data	CRU JRA (Harris, 2020)
PLUMBER2 & GLOBAL	global	1901–2018	atmospheric CO_2 concentration	Global Carbon Budget 2019 (Friedlingstein et al., 2019)
PLUMBER2 & GLOBAL	global	1901–2018	N deposition & P deposition	Lamarque et al. (2010, 2011)
PLUMBER2 & GLOBAL	global	1901–2018	Soil physical & chemical parameters	SoilGrid Hengl et al. (2017)
Remote sensing data				
PLUMBER2 & GLOBAL	global	2003–2011	MERIS-based RS chl_{leaf}	Croft et al. (2020)
PLUMBER2 & GLOBAL	global	2003–2011	GEOV1-based RS LAI	Baret et al. (2013)
FI-Sod	67.4°N, 26.6°E	2016–2020	Sentinel-3-based RS chl_{leaf}	Reyes-Muñoz et al. (2022)
US-NR1	40.0°N,-105.5°E	2019	Sentinel-3-based RS chl_{leaf}	Reyes-Muñoz et al. (2022)
***in-situ* observation data**				
PLUMBER2	global	1992–2018	eddy covariance CO_2 flux	Ukkola et al. (2022)
FI-Sod	67.4°N, 26.6°E	2015	chl_{leaf}	This paper (Peltoniemi et al., 2025)
FI-Sod	67.4°N, 26.6°E	2021–2024	fAPAR	Knorr et al. (2025)
US-NR1	40.0°N,-105.5°E	2017–2018	chl_{leaf}	Bowling and Logan (2019)
FI-Hyy	61.8°N, 24.3°E	June 2012	leaf C:N	TRY (Kattge et al., 2011)
US-MMS	39.3°N, -86.4°E	June 2014	leaf C:N	TRY (Kattge et al., 2011)
Feature importance additional data				
PLUMBER2 & GLOBAL	global	1989–2018	SPEI	global drought monitoring (Vicente-Serrano et al., 2023)

Table S2. Land cover (LC) classes used in the RS chl_{leaf} postprocessing. Based on ESA-CCI-LC documentation (ESA, 2017).

LC value	LC description	LC value	LC description
10	Cropland, rainfed	81	Tree cover, needle-leaved, deciduous, closed (>40%)
11	Herbaceous cover	82	Tree cover, needle-leaved, deciduous, open (15-40%)
20	Cropland, irrigated or post-flooding	90	Tree cover, mixed leaf type (broad-leaved and needle-leaved)
30	Mosaic cropland (>50%) / natural vegetation (tree, shrub, herbaceous cover) (<50%)	110	Mosaic herbaceous cover (>50%) /tree and shrub (<50%)
40	Mosaic natural vegetation (tree, shrub, herbaceous cover/ (>50%) / cropland (<50%)	120	Shrubland
50	Tree cover, broad-leaved, evergreen, closed to open	121	Evergreen shrubland
60	Tree cover, broad-leaved, deciduous, closed to open	122	Deciduous shrubland
61	Tree cover, broad-leaved, deciduous, closed	130	Grassland
62	Tree cover, broad-leaved, deciduous, open	140	Lichens and mosses
70	Tree cover, needle-leaved, evergreen, closed to open	150	Sparse vegetation (tree, shrub, herbaceous cover) (< 15%)
71	Tree cover, needle-leaved, evergreen, closed (>40%)	160	Tree cover, flooded, fresh or brakish water
72	Tree cover, needle-leaved, evergreen, open (15-40%)	180	Shrub or herbaveous cover, flooded, fresh/saline/brakish water
80	Tree cover, needle-leaved, deciduous, closed to open (>15%)		

Table S3. QUINCY plant functional types and the corresponding land cover (LC) types. The LC classes are listed in Table S2

Abbreviation	Long name	LC classes
BNE	Boreal needle-leaved evergreen	70, 71, 72, 90, 160
TeNE	Temperate needle-leaved evergreen	70, 71, 72, 90, 160
BNS	Boreal needle-leaved deciduous	80, 81, 82, 90, 160
TeBE	Temperate broad-leaved evergreen	40, 50, 90, 160
TeBS	Temperate broad-leaved deciduous	40, 60, 61, 62, 90, 160
TrBR	Tropical broad-leaved rain deciduous	60, 61, 62, 90, 160
TrBE	Tropical broad-leaved evergreen	50, 90, 160
TeC	C3 crops	10, 11, 20, 30, 110, 120, 121, 122, 130, 140, 150, 180
TeH	C3 grasslands	10, 11, 20, 30, 110, 120, 121, 122, 130, 140, 150, 180
TrH	C4 grasslands	10, 11, 20, 30, 110, 120, 121, 122, 130, 140, 150

Table S4. QUINCY leaf C:N lower and upper constraints, derived based on the TRY database (Kattge et al., 2011).

PFT	QUINCY leaf C:N lower boundary	QUINCY leaf C:N upper boundary
BNE	24	64.86
TeNE	24	64.86
BNS	16	30.97
TeBE	13.71	38.71
TeBS	13.71	38.71
TrBR	13.71	38.71
TrBE	13.71	38.71
TeC	13.71	40
TeH	13.71	40
TrH	17.14	48

Table S5. A list of QUINCY simulations

Name	Description	Sites
QUINCY default	default parametrization	PLUMBER2 & GLOBAL
QUINCY C_{only}	default parametrization, but C-cycle only enabled and with a fixed leaf stoichiometry	PLUMBER2
QUINCY $f_{\mathrm{N,chl}}$ increase	Same as QUINCY default, but $f_{\mathrm{N,chl}}$ increased by 30 %	PLUMBER2, only TeBS
QUINCY alter N frac	Same as QUINCY default, but leaf N allocation with the alternative scheme (see Section 2.1.2)	PLUMBER2
QUINCY alter N frac, $f_{\mathrm{N,rub}}$ increase	Same as QUINCY alter N frac, but $f_{\mathrm{N,rub}}$ increased by 30 %	PLUMBER2, only TeBS

Table S6. Random forest regression model preliminary training and preliminary testing coefficient of determination (R^2) scores.

PFT	QUINCY		Remote sensing	
	Train	Test	Train	Test
BNE	0.997	0.979	0.977	0.831
TeNE	0.997	0.981	0.934	0.498
BNS	0.979	0.861	0.963	0.515
TeBE	0.991	0.937	0.960	0.631
TeBS	0.985	0.890	0.977	0.820
TrBR	0.973	0.829	0.896	0.229
TrBE	0.974	0.821	0.980	0.867
TeC	0.967	0.764	0.959	0.730
TeH	0.980	0.864	0.973	0.828
TrH	0.930	0.499	0.948	0.643
all	0.971	0.790	0.961	0.727

Table S7. PFT means of chl_{leaf}, the 90th percentile of LAI, and GPP annual sums for the PLUMBER2 sites for QUINCY, remote sensing (RS), and flux tower observations of GPP. The numbers indicate the mean value of the site-level mean chl_{leaf} $\pm$ the standard deviation. Values are calculated based on site-level mean chl_{leaf} and GPP mean annual sum. Statistically significant ($p < 0.05$) correlation coefficients are marked with an asterisk. The PFT abbreviations are defined in Table 1.

PFT	chl_{leaf} ($\mu g\,cm^{-2}$)			LAI ($m^2\,m^{-2}$)			GPP ($gCm^{-2}yr^{-1}$)		
	QUINCY	RS	r	QUINCY	RS	r	QUINCY	Observations	r
BNE	44.4±9.4	41.3±25.4	0.66*	3.7±1.0	3.5±1.1	0.80*	935±365	1235±556	0.80*
TeNE	59.9±8.9	48.3±12.9	0.01	4.5±0.4	3.0±1.1	-0.48	1713±377	1805±241	0.30
TeBE	40.5±5.8	20.4±5.4	0.85	4.8±0.3	3.0±1.4	0.88	1970±350	1698±368	-0.37
TeBS	17.9±5.6	22.1±6.1	0.71*	4.1±0.6	4.4±1.5	0.42*	1231±366	1539±377	0.25
TrBR	26.4±13.7	10.2±0.0	-	4.6±1.2	1.9±1.1	-	1820±1019	1488±483	-
TrBE	45.7±9.0	55.8±13.2	0.22	4.7±0.2	4.5±1.3	0.42	2401±607	2445±872	0.64
TeC	13.7±1.4	28.4±10.4	0.11	4.5±1.8	3.3±1.2	-0.03	1437±469	1228±303	0.13
TeH	12.0±2.6	21.1±11.9	-0.04	3.1±1.9	2.6±1.5	0.55*	1004±545	977±687	0.77*
TrH	45.3±5.3	38.3±11.3	0.16	2.1±1.3	1.6±1.1	0.59*	756±416	902±502	0.52*
all	28.3±17.4	31.1±17.4	0.61*	3.7±1.6	3.1±1.6	0.51*	1229±620	1304±658	0.71*

Table S8. Group-based PFT means of chl_{leaf} and LAI 90th percentile time series for the PLUMBER2 and GLOBAL sites. The numbers indicate the mean value ± the standard deviation, and the minimum and maximum values are in parentheses. The values are calculated based on the site-level mean chl_{leaf} and LAI 90th percentile.

PFT	chl_{leaf} ($\mu g\,cm^{-2}$)		LAI ($m^2\,m^{-2}$)	
	QUINCY	Remote sensing	QUINCY	Remote sensing
BNE	39.0±7.0 (32.0–62.4)	33.1±17.9 (6.3–95.0)	3.1±1.1 (1.4–5.2)	3.5±1.0 (1.0–5.9)
TeNE	63.1±8.5 (38.9–71.9)	44.5±12.6 (20.5–74.5)	4.7±0.4 (3.7–5.0)	3.5±1.3 (0.4–5.6)
BNS	11.8±1.1 (10.5–12.9)	10.7±7.2 (4.0–20.4)	1.2±0.5 (0.5–1.7)	3.0±0.9 (2.1–4.4)
TeBE	42.3±5.4 (35.6–49.5)	22.7±8.6 (13.0–37.0)	4.9±0.4 (4.3–5.4)	3.3±1.2 (1.4–4.6)
TeBS	16.2±6.4 (5.3–32.8)	20.1±6.7 (6.7–35.5)	4.1±0.7 (1.0–5.0)	4.4±1.3 (1.2–6.3)
TrBR	20.6±10.4 (13.8–36.1)	13.2±3.5 (10.2–16.8)	4.1±0.9 (3.4–5.4)	2.7±1.1 (1.1–3.8)
TrBE	46.8±5.0 (33.0–59.7)	57.3±11.9 (26.4–78.7)	5.0±0.3 (4.2–5.5)	5.0±1.0 (2.0–6.1)
TeC	13.7±1.4 (10.5–16.7)	28.4±10.4 (13.2–46.3)	4.5±1.8 (1.9–7.3)	3.3±1.2 (1.5–5.2)
TeH	10.0±3.1 (4.6–17.2)	21.9±11.0 (2.0–47.1)	2.4±1.5 (0.4–7.9)	1.9±1.4 (0.2–5.5)
TrH	49.3±8.6 (31.9–71.8)	38.7±10.3 (12.2–62.4)	4.3±3.1 (0.6–12.2)	1.8±1.3 (0.1–5.4)
all	31.9±18.7 (4.6–71.9)	32.5±16.7 (2.0–95.0)	3.7±2.1 (0.4–12.2)	2.9±1.7 (0.1–6.3)

Table S9. The start of season (SOS), end of season (EOS) and length of season (LOS) for the PFT-averaged seasonal cycle of the PLUMBER2 Northern hemisphere TeBS sites.

Variable	chl_{leaf}		LAI		GPP	
	QUINCY	Remote sensing	QUINCY	Remote sensing	QUINCY	eddy covariance
SOS (DOY)	92	92	106	93	117	114
EOS (DOY)	347	337	347	317	309	283
LOS (days)	255	245	241	224	192	169

Table S10. The annual average chl_{leaf} ± std values and annual GPP sum for FI-Sod and US-NR1. DJF (December–February) and JJA (June–August) mean values are also listed. The numerical ranges are shown in parentheses after the annual means.

Sodankylä (FI-Sod)					
Variable	Season	QUINCY	RS, Croft et al. (2020)	RS, Sentinel-3	In-situ
chl_{leaf} ($\mu g\,cm^{-2}$)	yearly mean	35.0±1.2 (33–39)	18.4±4.7 (8–32)	16.1±9.3 (0–51)	57.9±10.4 (40–78)
chl_{leaf} ($\mu g\,cm^{-2}$)	DJF	33.9±0.3	18.2±3.8	-	-
chl_{leaf} ($\mu g\,cm^{-2}$)	JJA	36.1±0.6	20.1±5.0	21.2±6.7	62.6±7.8
GPP ($gC\,m^{-2}\,yr^{-1}$)	annual sum	545±52	-	-	602±82

Niwot-Ridge (US-NR1)					
Variable	Season	QUINCY	RS, Croft et al. (2020)	RS, Sentinel-3	In-situ
chl_{leaf} ($\mu g\,cm^{-2}$)	yearly mean	34.8±0.8 (33–38)	25.3±6.3 (7–52)	33.2±12.4 (3–56)	40.5±5.1 (27—46)
chl_{leaf} ($\mu g\,cm^{-2}$)	DJF	34.0±0.3	25.5±2.9	21.2±9.3	-
chl_{leaf} ($\mu g\,cm^{-2}$)	JJA	35.5±0.6	24.3±8.9	46.7±4.8	43.2±2.3
GPP ($gC\,m^{-2}\,yr^{-1}$)	annual sum	467±34	-	-	845±44

Table S11. PFT mean values for the mean chl_{leaf}, LAI 90th percentile and annual GPP for the PLUMBER2 sites with default QUINCY ("Q def."), QUINCY with alternative N fraction scheme ("Q alter N") and remote sensing (RS) and eddy flux covariance observations. $f_{N,struct}$ values are calculated as average JJA (June-August) fractions.

PFT	nr sites	$f_{N,struct}$ (-)		chl_{leaf} ($\mu g\,cm^{-2}$)			LAI ($m^2\,m^{-2}$)			GPP ($gC\,m^{-2}\,yr^{-1}$)		
		Q def.	Q alter N	Q def.	Q alter N	RS	Q def.	Q alter N	RS	Q def.	Q alter N	Obs
BNE	20	0.66	0.86	44.4±9.4	16.4±3.2	41.3±25.4	3.7±1.0	3.2±0.9	3.5±1.1	935±365	716±295	1235±556
TeNE	8	0.65	0.86	59.9±8.9	20.6±2.7	48.3±12.9	4.5±0.4	4.1±0.4	3.1±1.2	1713±377	1418±331	1805±241
TeBE	4	0.53	0.77	40.5±5.8	22.1±1.7	20.4±5.4	4.8±0.3	4.2±0.3	3.1±1.4	1970±350	1468±236	1698±369
TeBS	25	0.51	0.69	17.9±5.6	14.9±4.4	22.1±6.1	4.1±0.6	3.8±0.5	4.5±1.5	1231±366	1044±311	1539±377
TrBR	2	0.52	0.69	26.4±13.7	21.7±11.9	10.2±0.0	4.6±1.2	4.1±1.3	1.9±1.1	1820±1019	1553±977	1488±483
TrBE	9	0.58	0.76	45.7±9.0	26.6±4.7	55.8±13.2	4.8±0.2	4.5±0.2	4.6±1.3	2401±607	2125±585	2445±872
TeC	11	0.23	0.65	14.2±1.3	12.1±0.9	31.6±10.3	5.3±2.1	3.2±0.6	2.9±1.0	1569±505	790±171	1329±261
TeH	13	0.25	0.65	12.7±2.5	11.1±1.6	28.6±11.0	3.1±2.1	2.1±1.1	2.1±1.4	972±603	531±319	774±619
TrH	20	0.3	0.42	45.3±5.3	25.7±4.4	38.3±11.3	2.2±1.4	2.6±1.8	1.6±1.1	756±416	974±596	902±502
all	112	0.46	0.69	32.8±17.2	18.1±6.5	34.4±17.5	3.8±1.6	3.3±1.2	3.2±1.6	1262 ±648	1026±570	1358±664

Table S12. The mean chl_{leaf}, mean 90th percentile of LAI and annual GPP for the PLUMBER2 temperate broad-leaved deciduous (TeBS) sites for different QUINCY simulations and observations ± standard deviation between sites. In addition, the $f_{N,struct}$ for JJA mean are presented.

	$f_{N,struct}$ (-)	chl_{leaf} ($\mu g\,cm^{-2}$)	LAI ($m^2\,m^{-2}$)	GPP ($gC\,m^{-2}\,yr^{-1}$)
QUINCY default	0.51	17.9±5.6	4.1±0.6	1231±366
QUINCY default, 1.3x $f_{N,chl}$	0.50	24.6±7.6	4.0±0.5	1153±338
QUINCY alter N frac	0.69	14.9±4.4	3.8±0.5	1044±311
QUINCY alter N frac, 1.3x $f_{N,rub}$	0.60	18.5±5.7	4.0±0.5	1170±337
observations	-	22.1±6.1	4.5±1.5	1539±377

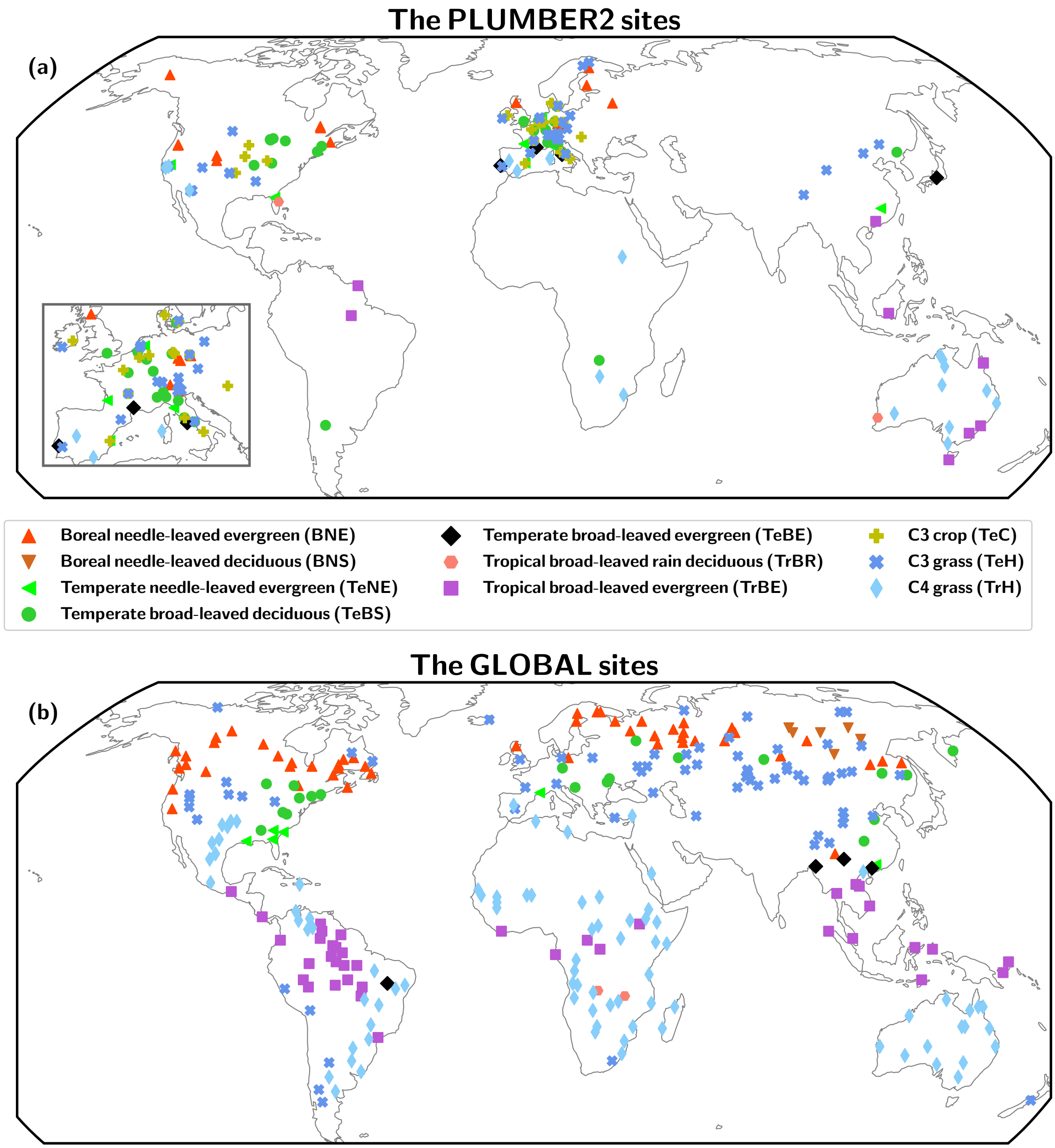

Figure S1. A map of the **(a)** PLUMBER2 sites and of the **(b)** GLOBAL sites. Different colors and markers indicate the PFT. A separate map of Europe is inserted in **(a)**.

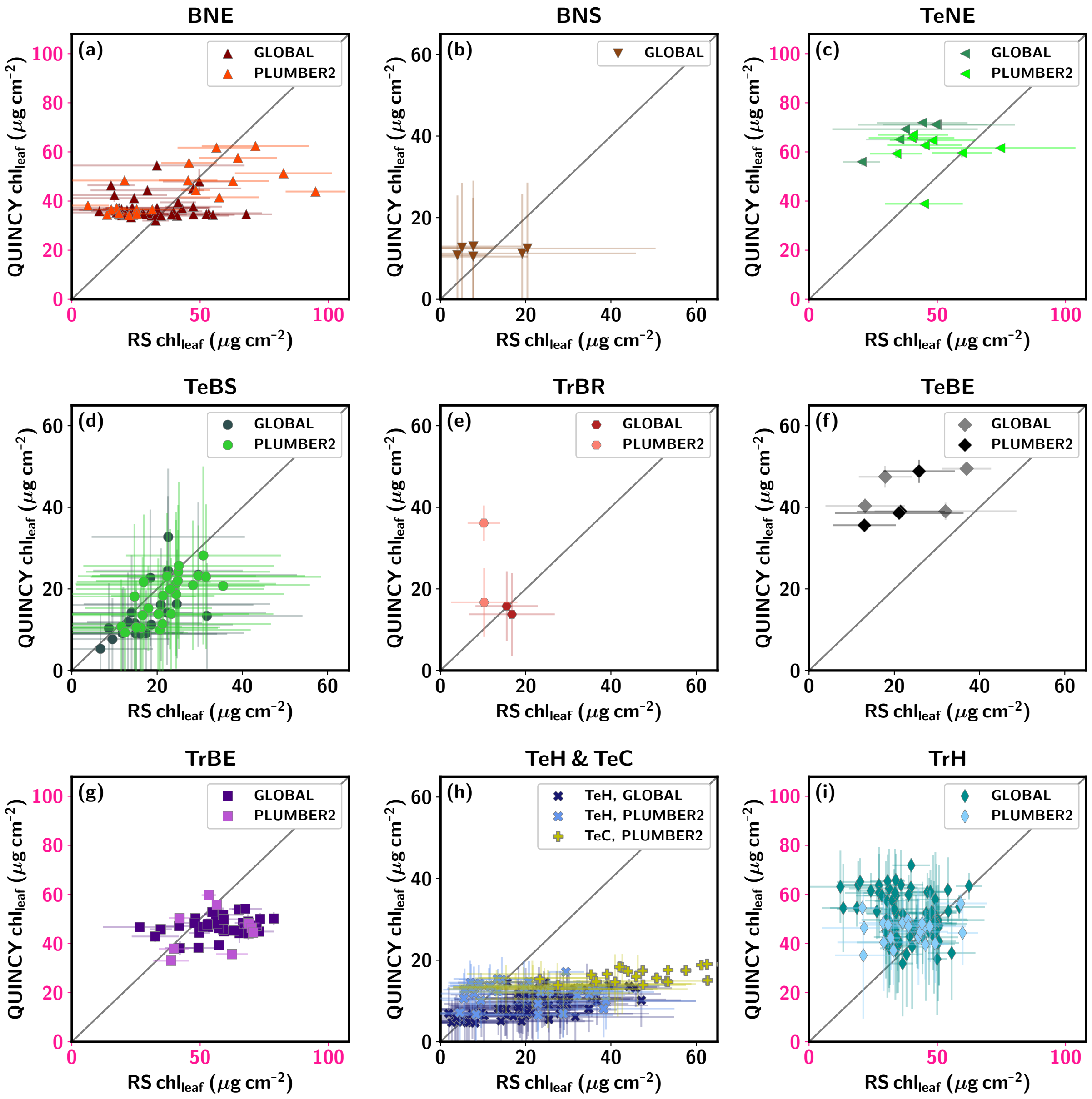

Figure S2. The mean site-level chl_{leaf} for the PLUMBER2 and GLOBAL sites for RS and QUINCY. Each marker represents one site. The whiskers show the mean interannual standard deviation for each site. Subplots **(a)**, **(c)**, **(g)** and **(i)** have a different scale on the x- and y-axis than the other subplots.

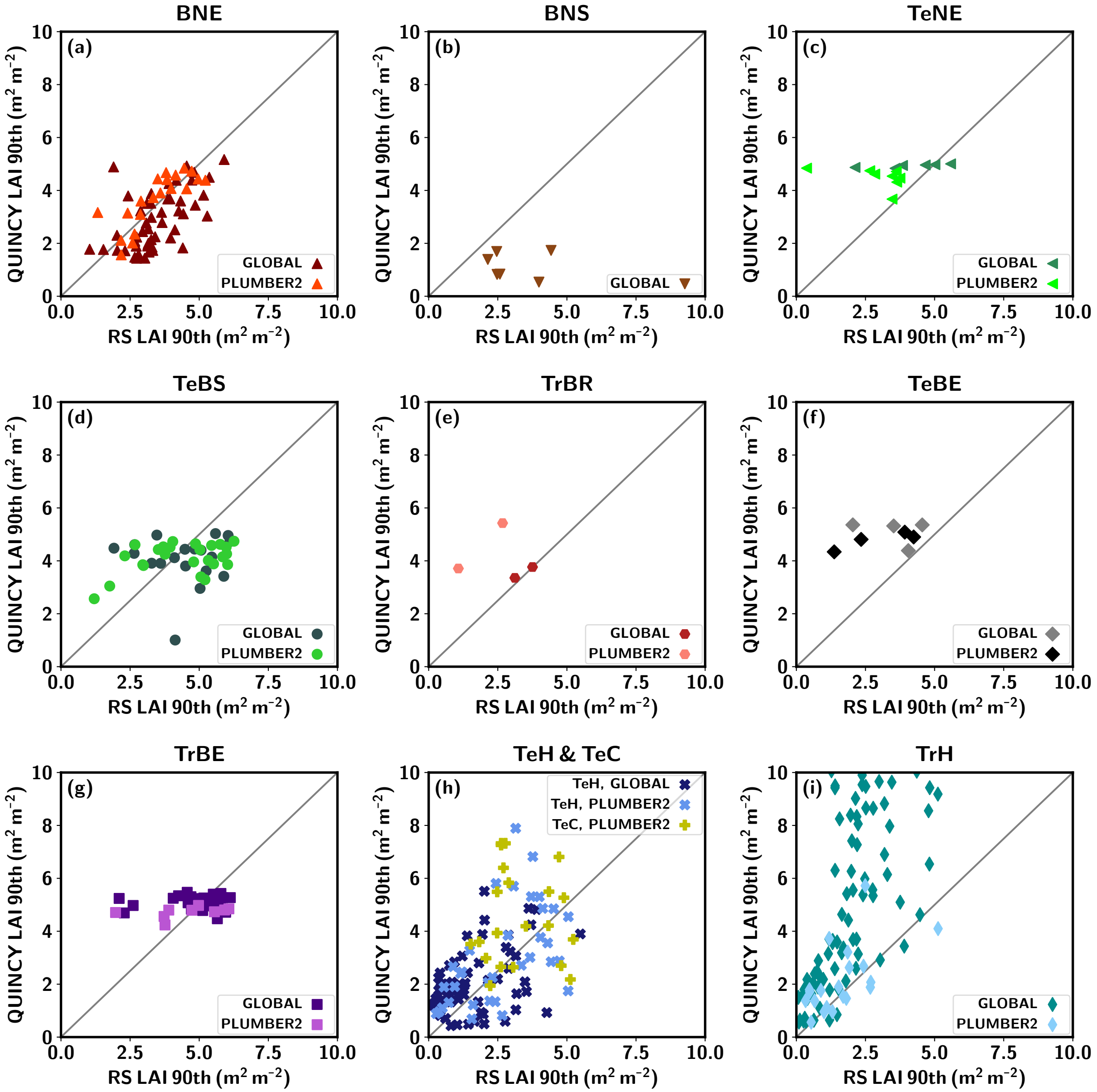

Figure S3. The site-level 90th percentiles of LAI for the PLUMBER2 and GLOBAL sites for RS and QUINCY.

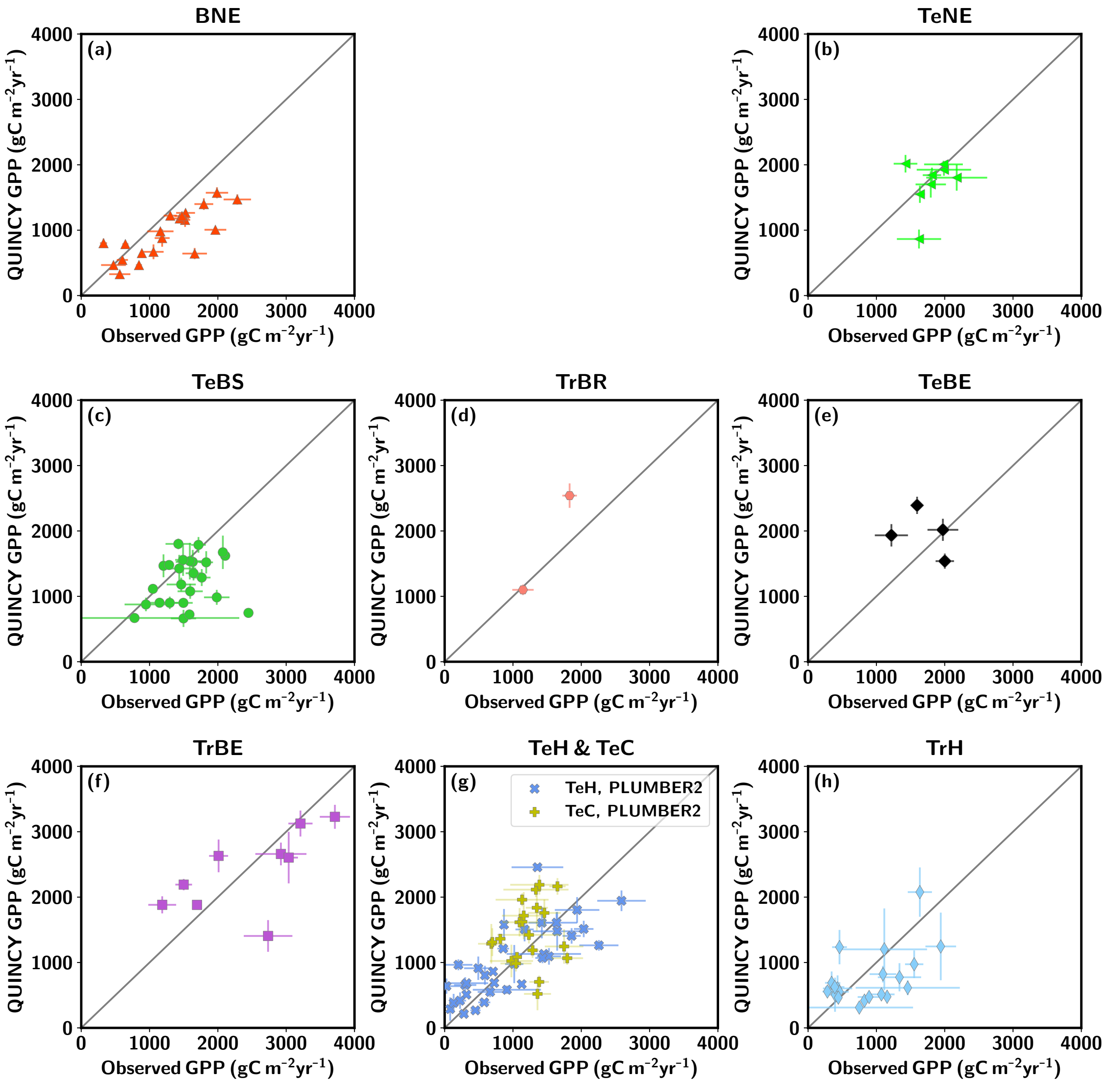

Figure S4. The mean annual GPP for different sites from the PLUMBER2 sites. The whiskers indicate the standard deviation calculated between annual GPP for different years. In the PLUMBER2 site set, there were no GPP ground observations for the boreal needle-leaved deciduous (BNS) PFT.

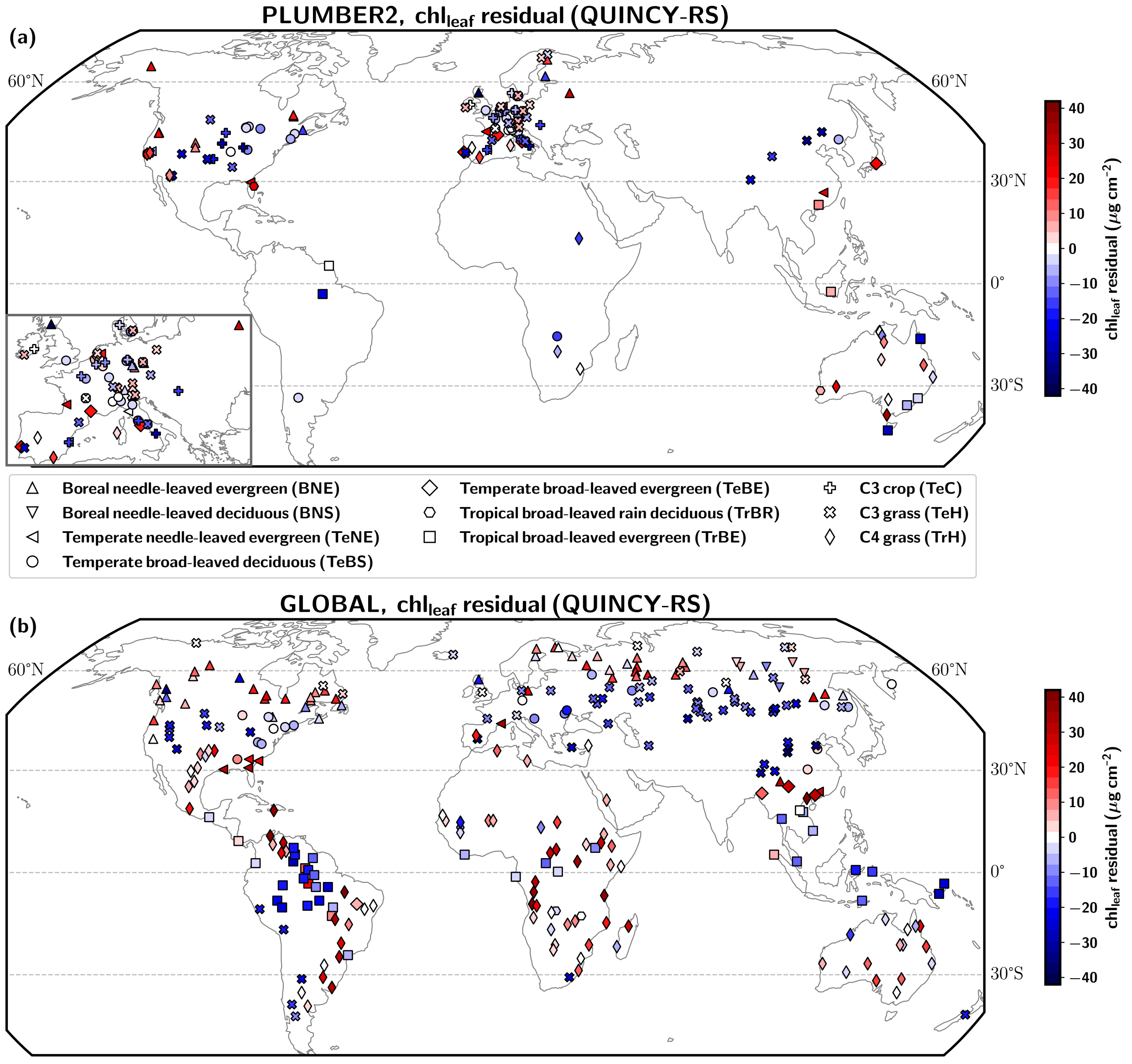

Figure S5. The residual chl_{leaf} between the mean values of QUINCY and RS for **(a)** PLUMBER2 and **(b)** GLOBAL sites. Each marker represents one site.

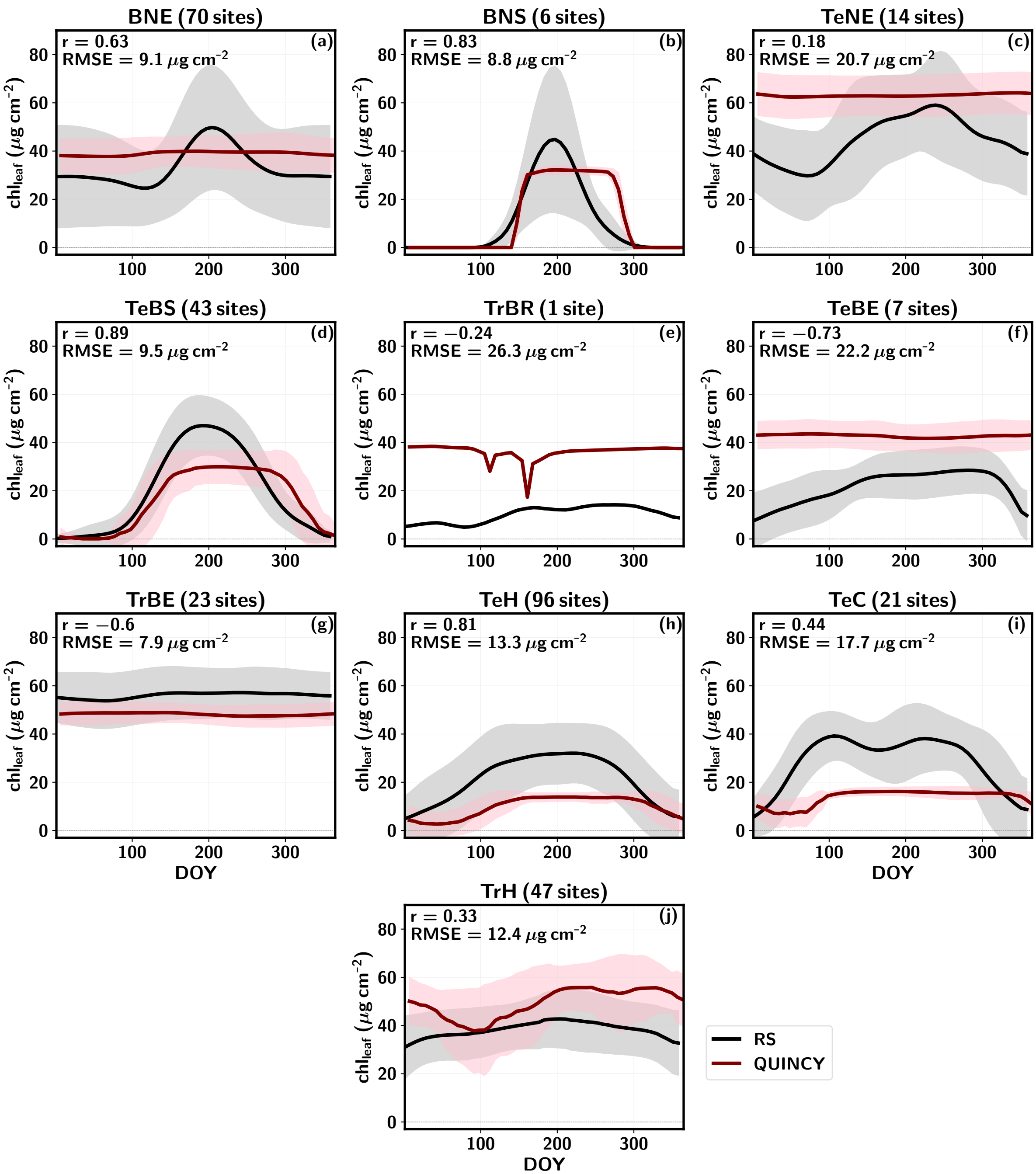

Figure S6. The PFT-averaged annual cycles of chl_{leaf} for the PLUMBER2 and GLOBAL Northern hemisphere sites for QUINCY (red line) and RS (black line). The shaded regions represent the standard deviation between sites. Depending on the site, the data is from years 1992-2018. The Pearson correlation (r) and root mean squared error (RMSE) are calculated between the mean QUINCY and RS PFT-averaged seasonal time series.

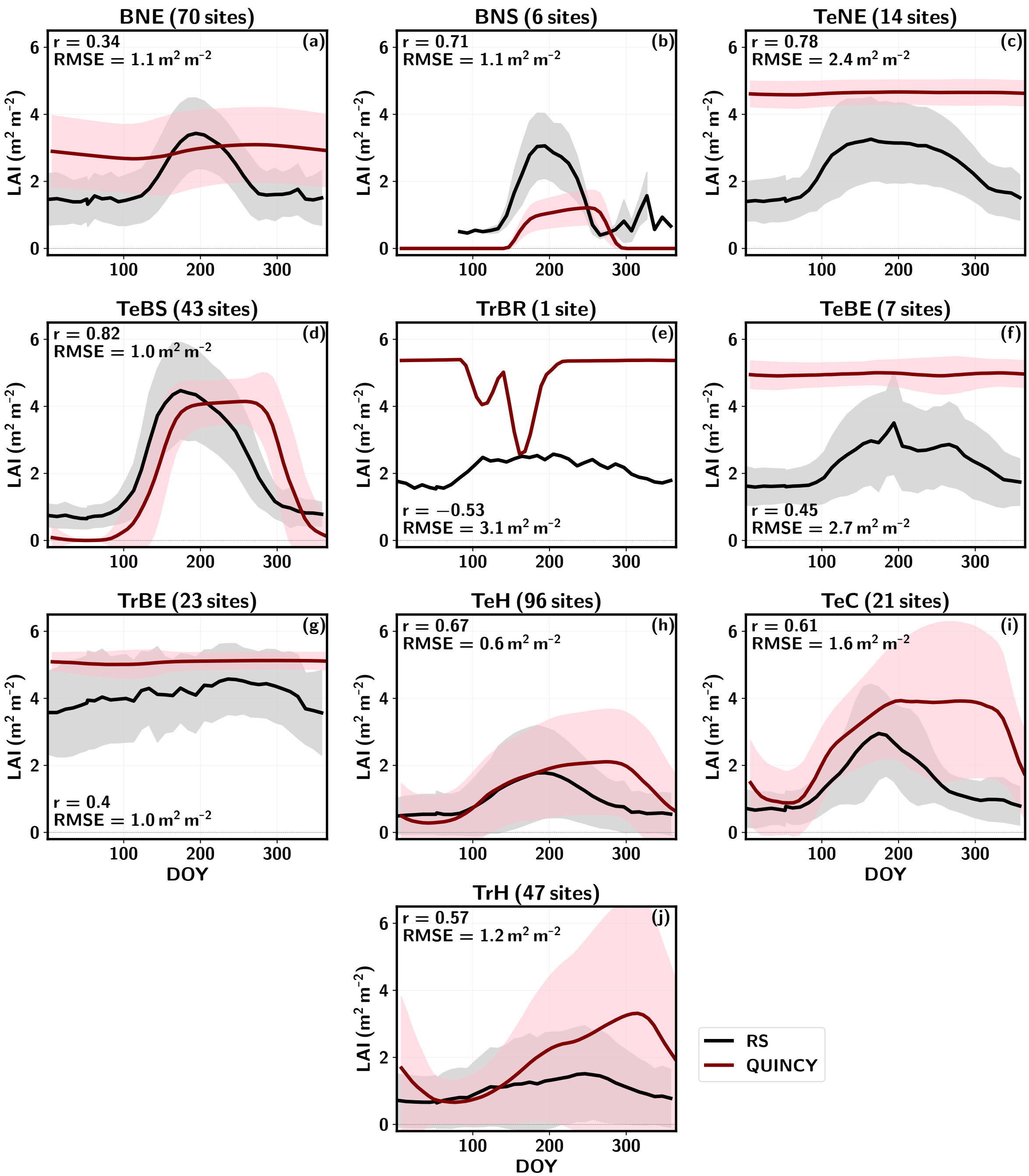

Figure S7. The PFT-averaged annual cycles of LAI for the PLUMBER2 and GLOBAL Northern hemisphere sites for QUINCY (red line) and RS (black line). The shaded regions represent the standard deviation between sites. Depending on the site, the data is from years 1992-2018. The Pearson correlation (r) and root mean squared error (RMSE) are calculated between the mean QUINCY and RS PFT-averaged seasonal time series.

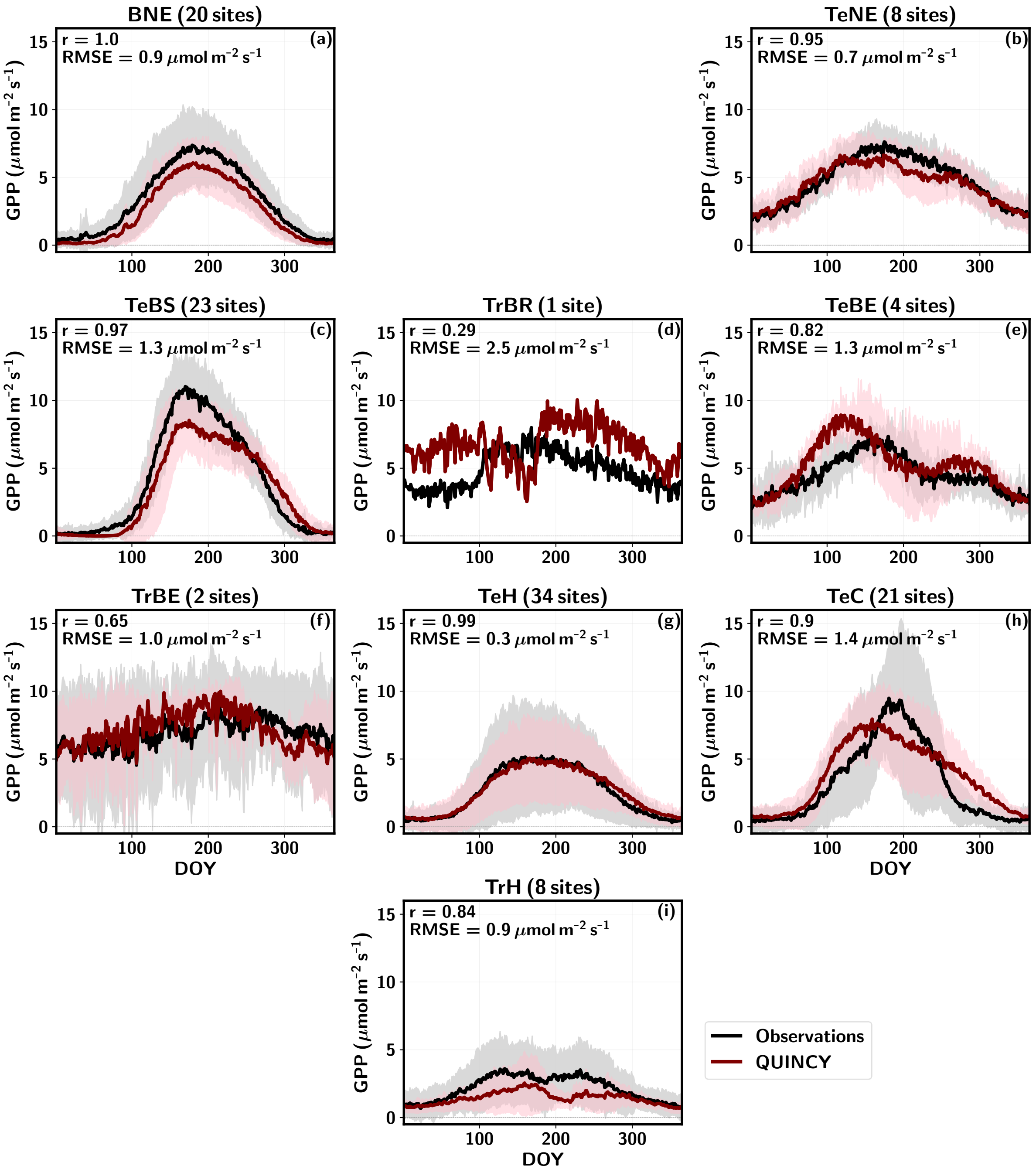

Figure S8. The PFT-averaged annual cycles of GPP for the PLUMBER2 Northern hemisphere sites for QUINCY (red line) and eddy covariance observations (black line). The shaded regions represent the standard deviation between sites. Depending on the site, the data is from years 1992-2018. The Pearson correlation (r) and root mean squared error (RMSE) are calculated between the mean QUINCY and observed PFT-averaged seasonal time series.

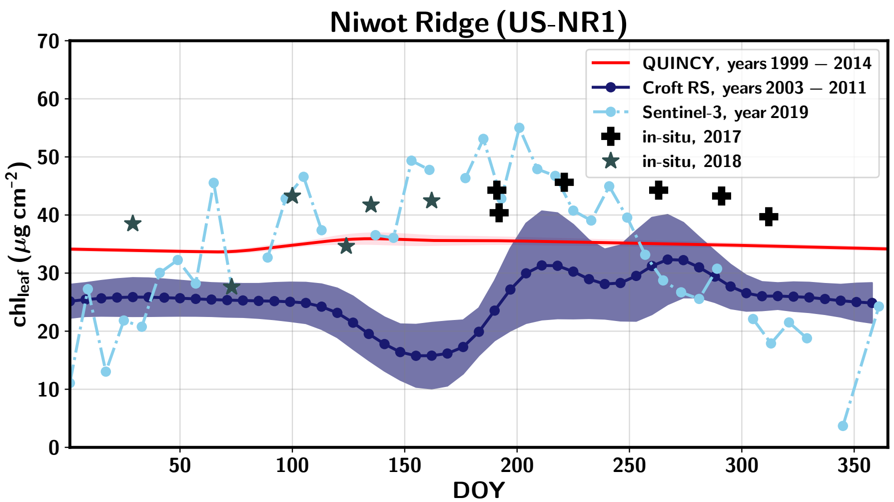

Figure S9. Seasonal cycle of daily averages for US-NR1 for chl_{leaf}. The shaded regions represent the standard deviation between years for QUINCY and RS data.

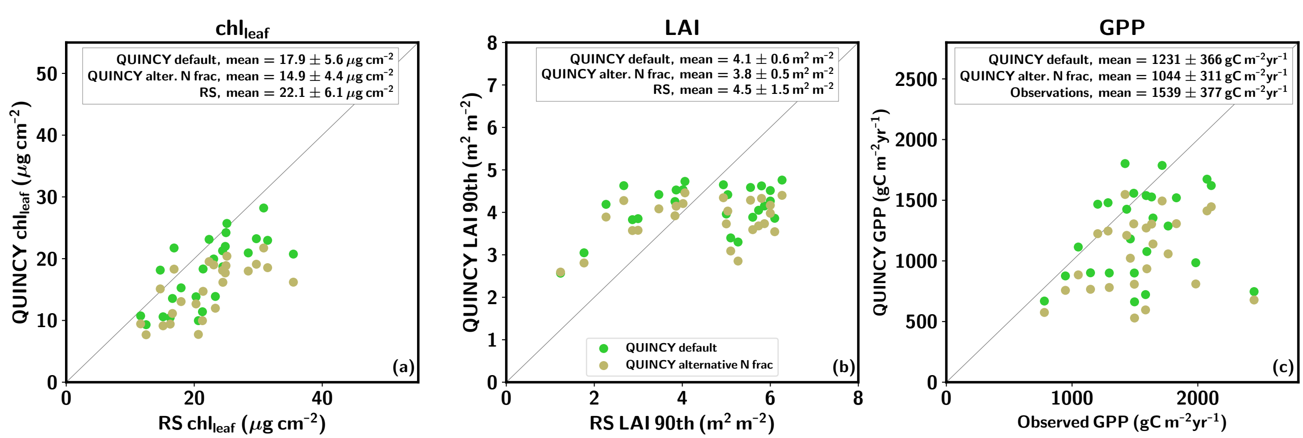

Figure S10. (a) The mean chl_{leaf}, **(b)** mean annual 90th percentile of LAI, and **(c)** annual GPP for the TeBS PLUMBER2 sites for QUINCY default and QUINCY alternative N fraction simulations and observations.

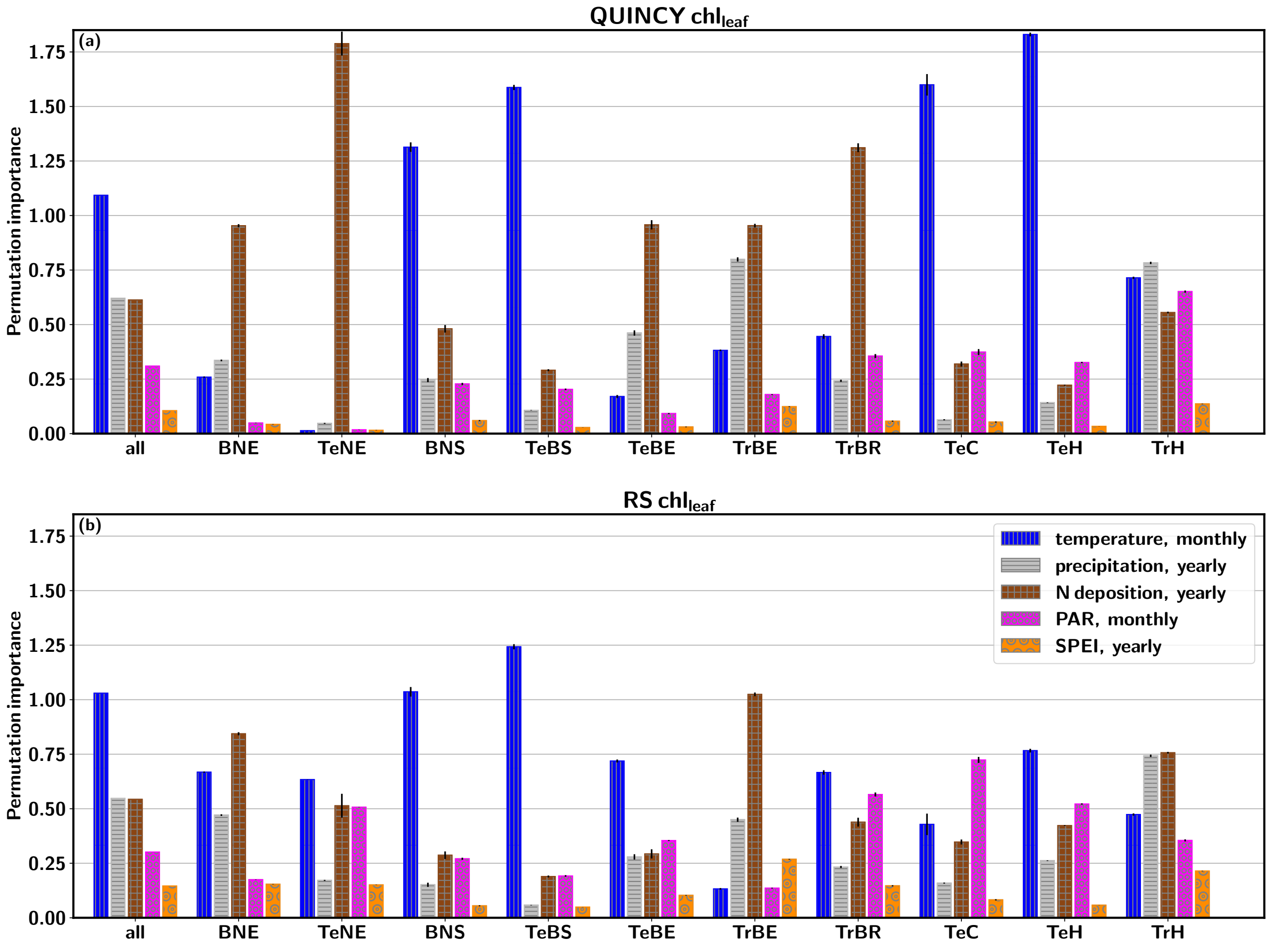

Figure S11. The permutation importance values for different PFTs after random forest regression fitting for **(a)** QUINCY chl_{leaf} and **(b)** RS chl_{leaf}.

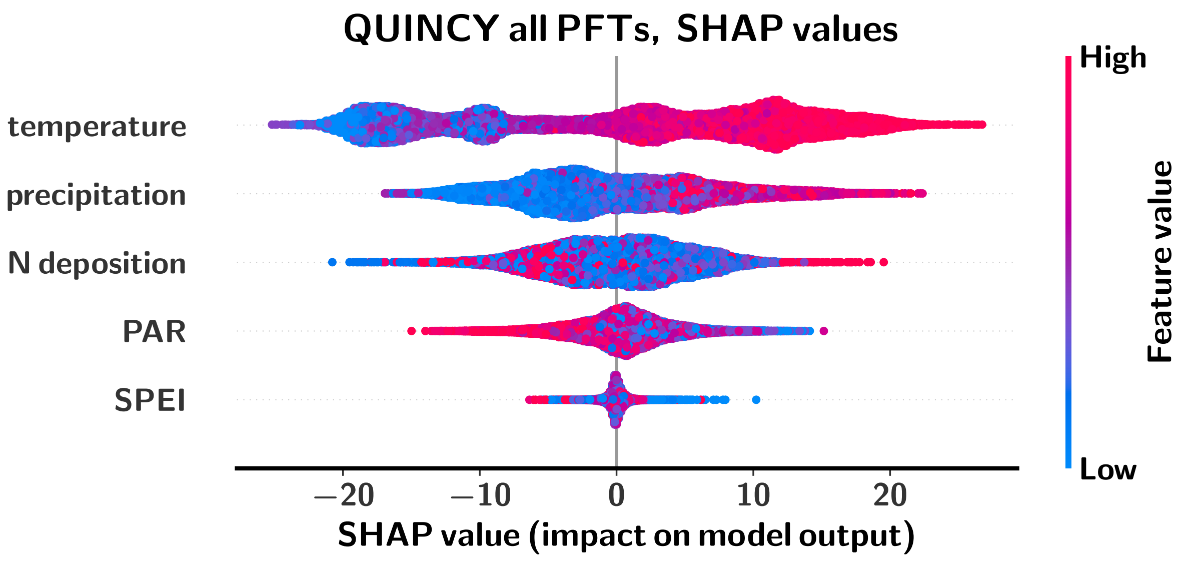

Figure S12. SHAP values of the random forest regression fit for the QUINCY chl_{leaf}, using three-month and annual averages. Each point represents a three-month average, and the color indicates the feature value. The more blue values correspond to low feature values, and the more red values correspond to high feature values.

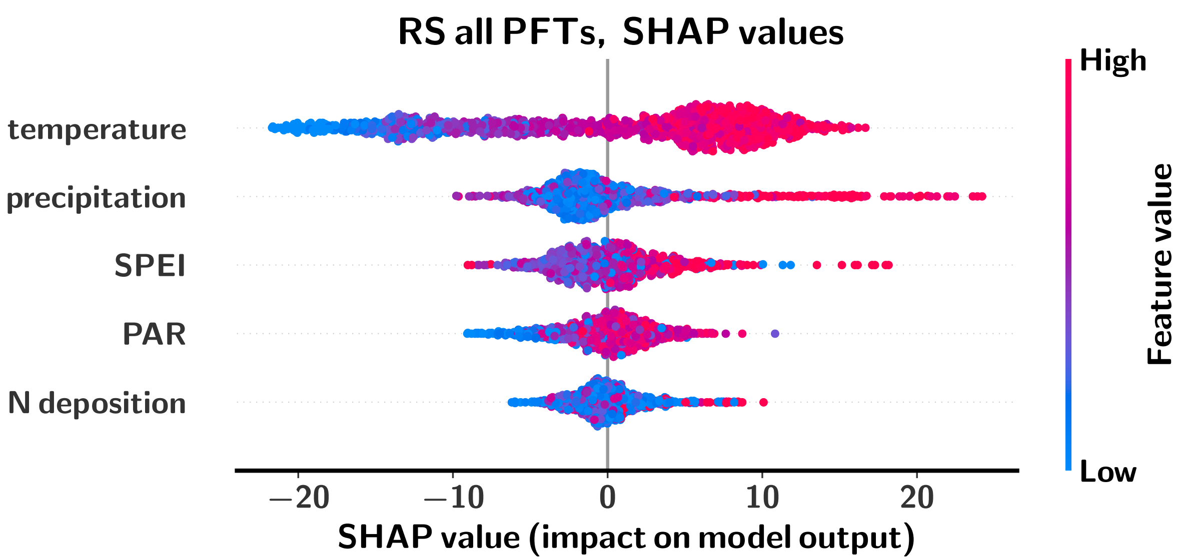

Figure S13. SHAP values of the random forest regression fit for the RS chl_{leaf}, using three-month and annual averages.

References

Baret, F., Weiss, M., Lacaze, R., Camacho, F., Makhmara, H., Pacholcyzk, P., and Smets, B.: GEOV1: LAI and FAPAR essential climate variables and FCOVER global time series capitalizing over existing products. Part1: Principles of development and production, Remote Sensing of Environment, 137, 299–309, https://doi.org/10.1016/j.rse.2012.12.027, 2013.

Bowling, D. and Logan, B.: Conifer Needle Pigment Composition, Niwot Ridge, Colorado, USA, 2017-2018, https://doi.org/10.3334/ORNLDAAC/1723, last access: February 17, 2025, 2019.

Croft, H., Chen, J., Wang, R., Mo, G., Luo, S., Luo, X., He, L., Gonsamo, A., Arabian, J., Zhang, Y., Simic-Milas, A., Noland, T., He, Y., Homolová, L., Malenovský, Z., Yi, Q., Beringer, J., Amiri, R., Hutley, L., Arellano, P., Stahl, C., and Bonal, D.: The global distribution of leaf chlorophyll content, Remote Sensing of Environment, 236, 111 479, https://doi.org/10.1016/j.rse.2019.111479, 2020.

ESA: Land Cover CCI Product User Guide Version 2. Tech. Rep., maps.elie.ucl.ac.be/CCI/viewer/download/ESACCI-LC-Ph2-PUGv2_2.0.pdf, last access: February 12, 2025, 2017.

Friedlingstein, P., Jones, M. W., O'Sullivan, M., Andrew, R. M., Hauck, J., Peters, G. P., Peters, W., Pongratz, J., Sitch, S., Le Quéré, C., Bakker, D. C. E., Canadell, J. G., Ciais, P., Jackson, R. B., Anthoni, P., Barbero, L., Bastos, A., Bastrikov, V., Becker, M., Bopp, L., Buitenhuis, E., Chandra, N., Chevallier, F., Chini, L. P., Currie, K. I., Feely, R. A., Gehlen, M., Gilfillan, D., Gkritzalis, T., Goll, D. S., Gruber, N., Gutekunst, S., Harris, I., Haverd, V., Houghton, R. A., Hurtt, G., Ilyina, T., Jain, A. K., Joetzjer, E., Kaplan, J. O., Kato, E., Klein Goldewijk, K., Korsbakken, J. I., Landschützer, P., Lauvset, S. K., Lefèvre, N., Lenton, A., Lienert, S., Lombardozzi, D., Marland, G., McGuire, P. C., Melton, J. R., Metzl, N., Munro, D. R., Nabel, J. E. M. S., Nakaoka, S.-I., Neill, C., Omar, A. M., Ono, T., Peregon, A., Pierrot, D., Poulter, B., Rehder, G., Resplandy, L., Robertson, E., Rödenbeck, C., Séférian, R., Schwinger, J., Smith, N., Tans, P. P., Tian, H., Tilbrook, B., Tubiello, F. N., van der Werf, G. R., Wiltshire, A. J., and Zaehle, S.: Global Carbon Budget 2019, Earth System Science Data, 11, 1783–1838, https://doi.org/10.5194/essd-11-1783-2019, 2019.

Harris, C.: CRU JRA v2.1: A forcings dataset of gridded land surfaceblend of Climatic Research Unit (CRU) and Japanese reanalysis (JRA) data, centre for Environmental Data Analysis, 2020.

Hengl, T., Mendes de Jesus, J., Heuvelink, G. B. M., Ruiperez Gonzalez, M., Kilibarda, M., Blagotić, A., Shangguan, W., Wright, M. N., Geng, X., Bauer-Marschallinger, B., Guevara, M. A., Vargas, R., MacMillan, R. A., Batjes, N. H., Leenaars, J. G. B., Ribeiro, E., Wheeler, I., Mantel, S., and Kempen, B.: SoilGrids250m: Global gridded soil information based on machine learning, PLOS ONE, 12, 1–40, https://doi.org/10.1371/journal.pone.0169748, 2017.

Kattge, J., Díaz, S., Lavorel, S., Prentice, I. C., Leadley, P., Bönisch, G., Garnier, E., Westoby, M., Reich, P. B., Wright, I. J., Cornelissen, J. H. C., Violle, C., Harrison, S. P., Van Bodegom, P. M., Reichstein, M., Enquist, B. J., Soudzilovskaia, N. A., Ackerly, D. D., Anand, M., Atkin, O., Bahn, M., Baker, T. R., Baldocchi, D., Bekker, R., Blanco, C. C., Blonder, B., Bond, W. J., Bradstock, R., Bunker, D. E., Casanoves, F., Cavender-bares, J., Chambers, J. Q., Chapin Iii, F. S., Chave, J., Coomes, D., Cornwell, W. K., Craine, J. M., Dobrin, B. H., Duarte, L., Durka, W., Elser, J., Esser, G., Estiarte, M., Fagan, W. F., Fang, J., Fernández-méndez, F., Fidelis, A., Finegan, B., Flores, O., Ford, H., Frank, D., Freschet, G. T., Fyllas, N. M., Gallagher, R. V., Green, W. A., Gutierrez, A. G., Hickler, T., Higgins, S. I., Hodgson, J. G., Jalili, A., Jansen, S., Joly, C. A., Kerkhoff, A. J., Kirkup, D., Kitajima, K., Kleyer, M., Klotz, S., Knops, J. M. H., Kramer, K., Kühn, I., Kurokawa, H., Laughlin, D., Lee, T. D., Leishman, M., Lens, F., Lenz, T., Lewis, S. L., Lloyd, J., Llusiá, J., Louault, F., Ma, S., Mahecha, M. D., Manning, P., Massad, T., Medlyn, B. E., Messier, J., Moles, A. T., Müller, S. C., Nadrowski, K., Naeem, S., Niinemets, Ü., Nöllert, S., Nüske, A., Ogaya, R., Oleksyn, J., Onipchenko, V. G., Onoda, Y., Ordoñez, J., Overbeck, G., Ozinga, W. A., Patiño, S., Paula, S., Pausas, J. G., Peñuelas, J., Phillips, O. L., Pillar, V., Poorter, H., Poorter, L., Poschlod, P., Prinzing, A., Proulx, R., Rammig, A., Reinsch, S., Reu, B., Sack, L., Salgado-negret, B., Sardans, J., Shiodera, S., Shipley, B., Siefert, A., Sosinski, E., Soussana, J.-f., Swaine, E., Swenson, N., Thompson, K., Thornton, P., Waldram, M., Weiher, E., White, M., White, S., Wright, S. J., Yguel, B., Zaehle, S., Zanne, A. E., and Wirth, C.: TRY – a global database of plant traits, Global Change Biology, 17, 2905–2935, https://doi.org/10.1111/j.1365-2486.2011.02451.x, 2011.

Knorr, W., Williams, M., Thum, T., Kaminski, T., Voßbeck, M., Scholze, M., Quaife, T., Smallman, T. L., Steele-Dunne, S. C., Vreugdenhil, M., Green, T., Zaehle, S., Aurela, M., Bouvet, A., Bueechi, E., Dorigo, W., El-Madany, T. S., Migliavacca, M., Honkanen, M., Kerr, Y. H., Kontu, A., Lemmetyinen, J., Lindqvist, H., Mialon, A., Miinalainen, T., Pique, G., Ojasalo, A., Quegan, S., Rayner, P. J., Reyes-Muñoz, P., Rodríguez-Fernández, N., Schwank, M., Verrelst, J., Zhu, S., Schüttemeyer, D., and Drusch, M.: A comprehensive land-surface vegetation model for multi-stream data assimilation, D&B v1.0, Geoscientific Model Development, 18, 2137–2159, https://doi.org/10.5194/gmd-18-2137-2025, 2025.

Lamarque, J.-F., Bond, T. C., Eyring, V., Granier, C., Heil, A., Klimont, Z., Lee, D., Liousse, C., Mieville, A., Owen, B., Schultz, M. G., Shindell, D., Smith, S. J., Stehfest, E., Van Aardenne, J., Cooper, O. R., Kainuma, M., Mahowald, N., McConnell, J. R., Naik, V., Riahi, K., and van Vuuren, D. P.: Historical (1850–2000) gridded anthropogenic and biomass burning emissions of reactive gases and aerosols: methodology and application, Atmospheric Chemistry and Physics, 10, 7017–7039, https://doi.org/10.5194/acp-10-7017-2010, 2010.

Lamarque, J.-F., Kyle, G. P., Meinshausen, M., Riahi, K., Smith, S. J., van Vuuren, D. P., Conley, A. J., and Vitt, F.: Global and regional evolution of short-lived radiatively-active gases and aerosols in the Representative Concentration Pathways, Climatic Change, 109, 191, https://doi.org/10.1007/s10584-011-0155-0, 2011.

Peltoniemi, M., Ruhanen, H., Linkosalmi, M., and Aurela, M.: Shoot pigment measurements from Scots pine trees at the Sodankylä eddy-covariance site in 2015, https://doi.org/10.5281/zenodo.17192030, 2025.

Reyes-Muñoz, P., Pipia, L., Salinero-Delgado, M., Belda, S., Berger, K., Estévez, J., Morata, M., Rivera-Caicedo, J. P., and Verrelst, J.: Quantifying fundamental vegetation traits over Europe using the Sentinel-3 OLCI Catalogue in Google Earth Engine, Remote Sensing, 14, https://doi.org/10.3390/rs14061347, 2022.

Ukkola, A. M., Abramowitz, G., and De Kauwe, M. G.: A flux tower dataset tailored for land model evaluation, Earth System Science Data, 14, 449–461, https://doi.org/10.5194/essd-14-449-2022, 2022.

Vicente-Serrano, S. M., Domínguez-Castro, F., Reig, F., Tomas-Burguera, M., Peña-Angulo, D., Latorre, B., Beguería, S., Rabanaque, I., Noguera, I., Lorenzo-Lacruz, J., and El Kenawy, A.: A global drought monitoring system and dataset based on ERA5 reanalysis: A focus on crop-growing regions, Geoscience Data Journal, 10, 505–518, https://doi.org/10.1002/gdj3.178, 2023.

Wellburn, A. R.: The Spectral Determination of Chlorophylls a and b, as well as Total Carotenoids, Using Various Solvents with Spectrophotometers of Different Resolution, Journal of Plant Physiology, 144, 307–313, https://doi.org/10.1016/S0176-1617(11)81192-2, 1994.